UiT
THE ARCTIC
UNIVERSITY
OF NORWAY

Department of Physics and Technology

Earth Observation Group

On the Generalized Curvature Ocean Surface Scattering Model for the NRCS and Doppler Frequency and its application to ocean surface wind retrieval from Synthetic Aperture Radar data

—

Faozi Saïd

A dissertation for the degree of Philosophiae Doctor – January 2015

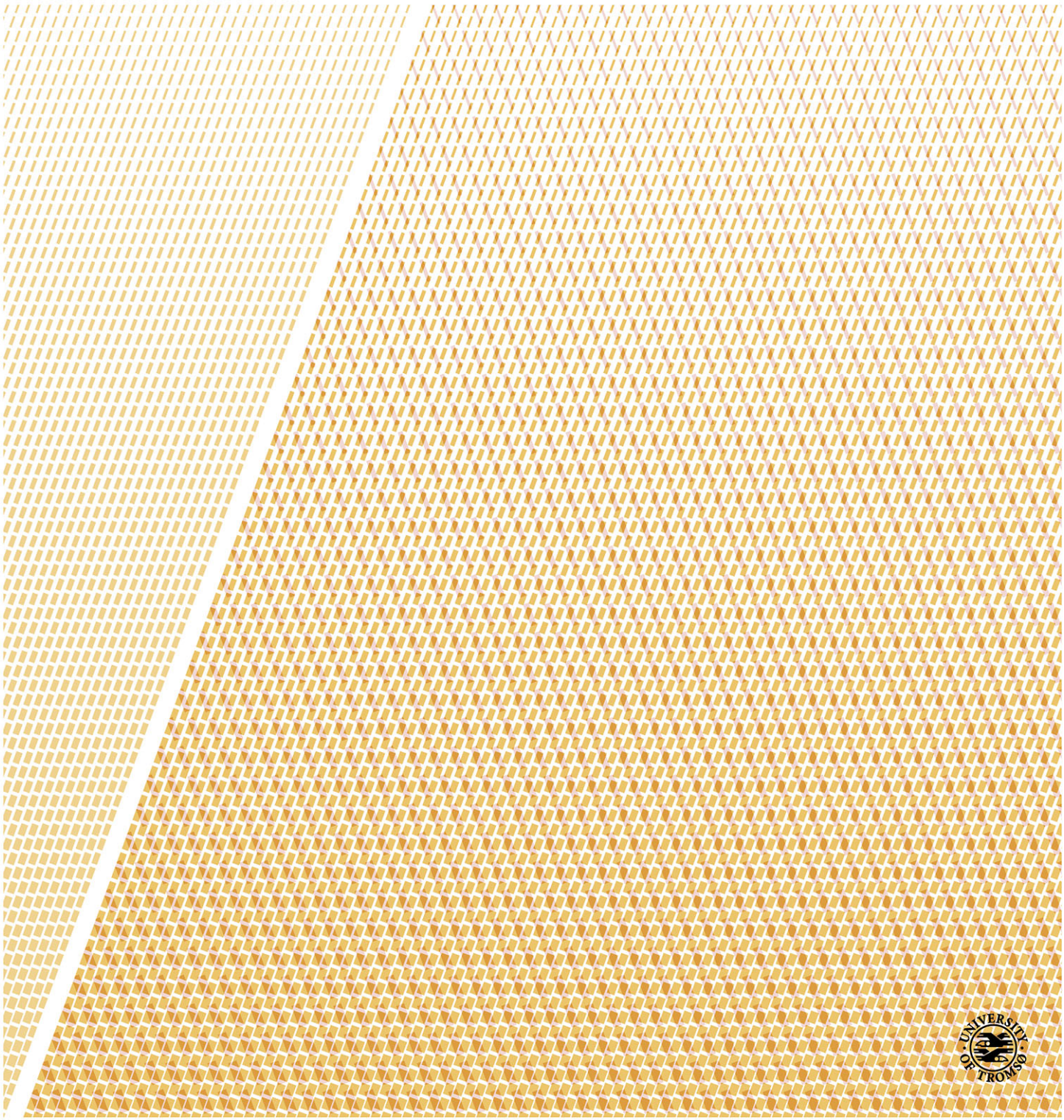

To my family and friends from French Polynesia

«The principles of living greatly include
the capacity to face trouble with courage,
disappointment with cheerfulness,
and trial with humility.»
Thomas S. Monson

Abstract

A sea surface wind retrieval technique using X-band dual-polarized SAR stripmap (SM) data is first presented in this thesis. This method combines the use of retrieved normalized radar cross section (NRCS) measurements at **hh** and **vv** polarizations, with the polarization residual Doppler frequency (PRDF)–the difference between the **vv** and **hh** Doppler centroids ($\mathbf{D_c}$). Geophysical model functions (gmfs) used for the inversion procedure are based on the generalized curvature ocean surface scattering model [general curvature model (GCM)], namely the GCM-NRCS and GCM-Dop. Using a series of carefully selected dual-polarized SM TerraSAR-X scenes along the Norwegian coast, a 1.13 m/s bias, with a correlation of 0.85 and a 1.86 m/s rmse, is found between the mean estimated wind speeds and *in situ* measurements; a 15.43 deg bias, with a 0.93 correlation and a 34.1 deg rmse exists between the mean estimated wind directions and *in situ* measurements. The GCM-NRCS and GCM-Dop gmfs are both extended and revisited. First a sea surface spectrum undressing procedure is implemented with the addition of a skewness phase related component based on empirical skewness coefficients of sea surface slope pdf. Using the GCM-NRCS gmf, NRCS simulations are then generated at C-band for various wind conditions, polarizations, and incidence angles, and compared against CMOD5.n. The use of an undressed sea surface spectrum affects the NRCS dynamic mostly in low wind conditions ($\leq$5 m/s). The inclusion of the skewness phase related component helps improve the up/down wind asymmetry particularly for moderate winds ($\approx$ 5-10 m/s) and moderate incidence angles ($\approx$ 32-40 degrees). The GCM-Dop gmf performance is gauged against the empirical CDOP gmf. For wind speeds less than 10 m/s, the skewness phase related component is included while effects from wave breaking are implemented for wind speeds greater than 10 m/s. As with the GCM-NRCS gmf, simulated $\mathbf{D_c}$ values are generated for **hh** and **vv** polarizations, various wind conditions, and incidence angles, and compared with CDOP. Overall bias for simulated $\mathbf{D_{c-hh}}$ with and without skewness are 2.63 vs. -0.51 Hz, respectively; overall standard deviations are 2.76 vs. 3.53 Hz. For simulated $\mathbf{D_{c-vv}}$, overall bias values with and without skewness are -0.16 vs. -2.52 Hz; standard deviations are 3.56 vs 4.32 Hz. When considering the wave breaking component for wind speeds greater than 10 m/s, the overall bias for simulated $\mathbf{D_{c-hh}}$ with and without it are -0.08 vs. 0.12 Hz, respectively; corresponding standard deviations are 3.32 vs. 4.75 Hz. Bias values for simulated $\mathbf{D_{c-vv}}$ with and without the wave breaking component are -1.83 vs. -2.02 Hz, with corresponding overall standard deviations of 3.43 vs. 4.87 Hz. The largest deviation from CDOP, of about 18 Hz, is found in the up-wind direction for a 26 degree incidence angle, 10 m/s wind speed, and **hh** polarization.

Acknowledgments

I would like to first thank Harald Johnsen and Torbjørn Eltoft for their constant support and trust throughout this whole process. They have always made themselves available when the need arose. I would also like to thank Yngvar Larsen from Norut for all the answers and help he provided while I was working at Norut. I would also like to acknowledge the 'French team' at Ifremer in Brest-France, for the numerous scientific conversations we had, namely, Bertrand Chapron, Fabrice Collard, Alexis Mouche, Frédéric Nouguier, and Gilles Guitton. We have all become good friends, and may probably collaborate at times in future scientific projects. Finally, I would like to say a big thank you to my wife for her endless support throughout these four years. She has been very patient, supportive, and believed in my success. Thank you Laina.

Contents

List of Tables

List of Figures

Chapter 1

Introduction

This chapter provides a motivation summary on the potential use of synthetic aperture radar (SAR) instruments to infer sea surface winds from space, and the improvement of a backscatter and Doppler models based on the electromagnetic scattering model from [Engen et al., 2006]. Chapter and publication reviews are also provided in a separate section.

1.1 Motivation

Ocean wind monitoring is an integral part of weather forecasting, maritime shipping lane planning, offshore wind research, as well as the study of climate patterns. Current methods used to endeavor such an important and complex task mostly rely upon satellite radar instruments, and buoy stations carefully placed within the various ocean basins. Satellite radar instruments have the major advantage of increased spatial coverage compared to buoy stations. Two major classes of radar instruments are used to measure geophysical parameters, namely passive and active. Passive remote sensors are designed to detect natural energy emitted from the earth surface, while active remote sensors are designed to transmit electromagnetic waves toward the earth surface, and record the backscatter energy. Scatterometers and synthetic aperture radar (SAR) constitute the majority of such active sensors. Scaterrometers are primarily designed for high spatial coverage at the price of lower spatial resolution; while SAR instruments provide very high spatial resolution at the cost of lower spatial coverage.

The backscatter energy from either of these active sensors can be exploited to retrieve ocean sea surface winds using semi-empirical geophysical model functions (GMFs). Since scaterrometers are usually the tool of choice for global ocean monitoring, most GMFs have been developed for such radars. It is however possible to modify a scatterometer specific GMF to work with a given SAR instrument. The SAR instrument also offers the unique possibility of using other metrics for sea surface wind retrieval such as the Doppler anomaly, in combination with backscatter measurements.

In this thesis, we desire to focus on the potential use of SAR instruments in sea

surface wind retrievals. To do so, we present an alternative approach using both the normalized radar cross section (NRCS) and Doppler centroid (D_c) measurements as key radar parameters to infer wind measurements from SAR stripmap backscatter data. Such a procedure is made possible using both a backscatter and Doppler models based on the electromagnetic scattering model from [Engen et al., 2006]. In fact, these GMFs are revisited and improved in this thesis, where a more realistic sea surface description is included.

1.2 Chapter and Publication Review

Chapter 2 introduces basic SAR theory principles, such as SAR geometry, and the SAR signal. A specific subsection is also dedicated to the Doppler centroid since the latter can play a major role in SAR ocean wind retrievals. Sea surface scattering basics are also discussed, along with common sea surface wind retrieval techniques. Finally, a specific SAR ocean wind retrieval procedure combining the use of both the normalized radar cross section and the Doppler centroid is presented. A detailed description of the backscatter and Doppler models based on the generalized curvature model (GCM) [Engen et al., 2006] is also included.

Chapter 3 refers to a paper entitled "Ocean Surface Wind Retrieval From Dual-Polarized SAR Data Using the Polarization Residual Doppler Frequency" by F. Said and H. Johnsen, published in the IEEE Transactions on Geoscience and Remote Sensing (volume 52, issue 7) in September 2013. This paper explores the potential use of both the normalized radar cross section (NRCS) and the polarization residual Doppler frequency (PRDF)–the difference between the *VV* and *HH* Doppler centroids—in sea surface wind retrieval using SAR stripmap data. The use alone of NRCS SAR measurements makes it near impossible to successfully retrieve sea surface winds, without the use of ancillary data. When combined with Doppler centroid measurements, the number of wind ambiguities decreases significantly. The use of the PRDF enables the elimination of unwanted biases usually present in both *VV* and *HH* Doppler estimates.

The presented study is performed at X-band using a series of dual-polarized stripmap TerraSAR-X scenes along the Norwegian coast. Wind measurements are inferred from measured NRCS and PRDF using two related geophysical model functions both based on the general curvature model (GCM) [Engen et al., 2006], namely the GCM-NRCS and GCM-Dop. Inferred wind measurements are compared with *in situ* measurements. A 1.13-m/s bias, with a correlation of 0.85 and a 1.86-m/s rmse, are found between the mean estimated wind speeds and *in situ* measurements; while a 15.43 degrees bias with a 0.93 correlation coefficient and a 34.1 rmse exist between estimated and *in situ* measurements.

Chapter 4 refers to a paper entitled "Onto a skewness approach to the generalized curvature ocean surface scattering model" by F. Said, H. Johnsen, Frédéric Nouguier, Bertrand Chapron, and Geir Engen. This paper has been submitted to the IEEE Trans-

actions on Geoscience and Remote Sensing. Chapter 4 explores the GCM-NRCS GMF first introduced in [Engen et al., 2006]. The purpose of this paper is to improve and provide a more realistic NRCS model by including a necessary sea surface spectrum undressing procedure, as well as a skewness phase related component. The paper first discusses the general use of GMFs in sea surface wind retrievals. A high level description of the original GCM-NRCS GMF from [Engen et al., 2006] is provided, followed by the implementation of the skewness related phase component and the inclusion of the sea surface spectrum undressing procedure. The improved version of the GCM-NRCS GMF is then compared against the CMOD5.n GMF. Simulations are performed for various wind conditions, polarizations, and incidence angles. Although necessary, the inclusion of the sea surface spectrum undressing step has a small impact on the NRCS dynamic, mostly noticeable in low wind conditions (less than 5 m/s). The skewness phase related component does affect however the up/down wind asymmetry which was otherwise absent in the GCM-NRCS GMF; good agreement is found between the extended version of the GCM and CMOD5.n for moderate winds (5-10 m/s), and moderate incidence angles (32-40 degrees). The GCM-NRCS GMF tends to overestimate the up/down wind asymmetry for low incidence angles (less 26 degrees), compared to CMOD5.n.

Chapter 5 refers to a paper entitled "An ocean wind Doppler model based on the generalized curvature ocean surface scattering model" by F. Said, H. Johnsen, Bertrand Chapron, and Geir Engen. This paper has also been submitted to the IEEE Transactions on Geoscience and Remote Sensing. Preliminary work on a Doppler model based on the GCM were first presented in an Envisat and ERS symposium in 2004 [Pedersen et al., 2004]. This chapter builds on this work by first providing a high level description of the GCM-Dop, and introducing two new key components included in the model namely the skewness related phase and wave breaking D_c components. The use of these two variables provides a more realistic Doppler centroid model when compared to the semi-empirical CDOP GMF. In fact, a simulation analysis is provided in the paper where the two models are compared for various wind conditions and incidence angles, and *HH* and *VV* polarizations. Up/down wind asymmetry is now present in the improved version of the GCM-Dop, although noticeable overestimation of the D_c is seen in the up-wind direction for wind speeds between 7 and 10 m/s, incidence angles less than 32 degrees, and for both polarizations. We also note an underestimation of about 5 Hz around the up-wind direction for a 40 degree incidence angle at *vv* polarization compared to CDOP. Overall simulation results against CDOP are nonetheless promising.

Chapter 6 concludes by recalling the various contributions from this thesis. A future work discussion is also included in this chapter.

1.3 Other Publications and Presentations

- F. Said and H. Johnsen, "Validation of the Generalized Curvature Ocean Surface Scattering Model against dual pol RADARSAT-2 and TerraSAR-X data", *poster*

presentation given at 2nd Nordic Remote Sensing Days, Aug 2011, Troms, Norway

- F. Said and H. Johnsen, "Assessment of ocean wind retrieval from dual-polarized x-band SAR data", *Proc. 9th EUSAR*, Apr. 2012, pp. 653–656.
- F. Said and H. Johnsen, "Sea surface wind retrieval using both normalized radar cross section and polarization residual doppler frequency from TerraSAR-X data", *Geoscience and remote Sensing Symposium (IGARSS), 2012 IEEE International*, July 2012, pp. 2063–2066.

Chapter 2

Background

2.1 SAR theory

While scatterometer instruments are one of the most widely used type of radars for ocean wind studies, there is an increased interest in the use of SAR instruments partly due to their ability in detecting mesoscale to sub-mesoscale features [Ainsworth et al., 1995] [Collard et al., 2008], and better performance in coastal areas [Christopher R. Jackson, 2004a]. Prior to discussing how SAR data can be used in sea surface wind studies, a high level description on how SAR instruments operate and acquire data is provided.

2.1.1 SAR geometry

In order to understand how a SAR instrument operates, an illustration of its data acquisition geometry is provided. Figure 2.1 shows a simple geometric model of a monostatic SAR instrument with its beam footprint over a static point target. Here, we define some of the key components shown in this figure:

- the nadir point corresponds to the location directly below the radar on the Earth's surface
- as the sensor moves, the nadir point draws a line on the ground called the radar track
- the azimuth direction is parallel to the sensor path while the range direction is perpendicular to it
- the beam footprint corresponds to the 3 dB projection of the transmitted radar antenna beam onto the ground surface
- the slant range (R) is the distance between the target and the radar measured along the radar line-of-sight
- the range of closest approach is represented by R_o

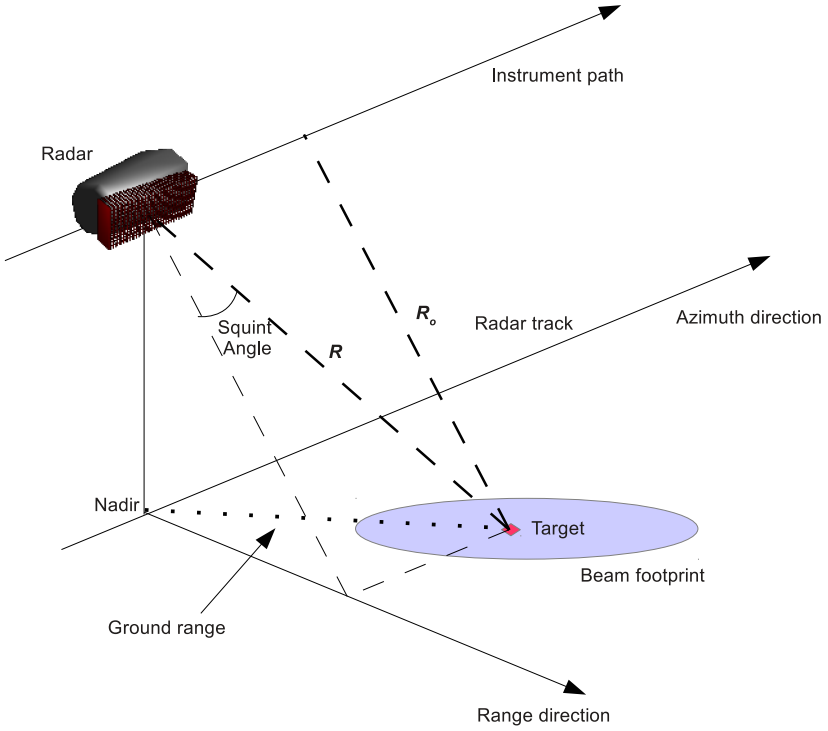

Figure 2.1: Graphical representation of a SAR data acquisition geometry. R and R_o represent the slant-range distance and range of closest approach, respectively.

- the squint angle corresponds to the angle between R and R_o
- the distance between nadir and the target is called ground range

One of the most important SAR parameters is the slant range R. Its precise mathematical description is essential in providing accurate expressions of both transmitted and received SAR signals. As the sensor moves along its path, the range R varies and is defined using the so-called range equation. Assuming a non-rotating flat Earth in proximity to the target with an appropriate choice for the sensor velocity, a simple model can be used to solve for the range equation [Cumming and Wong, 2005]. Let V_r be the effective sensor velocity on the ground, η the azimuth time referenced to the time of closest approach; solving for R gives

$$R^2(\eta) = R_o^2 + (V_r\eta)^2. \tag{2.1}$$

Equation (2.1) is called the hyperbolic form of the range equation. As previously mentioned, this equation provides a critical component to precise solving of the SAR signal.

2.1.2 SAR signal

In general a SAR instrument transmits in range a linear frequency modulated (FM) pulse of the form

$$s_t(\tau) = \omega_r(\tau)\cos(2\pi f_o\tau + \pi K_r\tau^2), \tag{2.2}$$

where ω_r represents the pulse envelope, f_o is the carrier operating frequency, τ is the range time, and K_r is the FM rate of the range pulse. The pulse envelope is usually approximated to be rectangular such that

$$\omega_r(\tau) = rect(\frac{\tau}{T_r}), \tag{2.3}$$

where T_r is the pulse duration. If such a signal bounces from a point target on the ground at a distance R from the radar, the received signal $s_r(\tau)$ at the SAR antenna is then the convolution of the transmitted FM pulse with the target reflectivity $g_{tar}(\tau)$

$$s_r(\tau) = s_t(\tau) * g_{tar}(\tau), \tag{2.4}$$

with

$$g_{tar}(\tau) = A_t\delta(\tau - 2R/c), \tag{2.5}$$

where A_t and c represent the magnitude of the backscatter signal from the point target, and the speed of light, respectively. Note that $2R/c$ represents the time it takes for the transmitted SAR signal to travel to and from the target. Inserting (2.2) and (2.5) into (2.4), the received signal becomes

$$s_r(\tau) = A_t\omega_r(\tau - 2R/c)\cos(2\pi f_o(\tau - 2R/c) + \pi K_r(\tau - 2R/c)^2 + \gamma), \tag{2.6}$$

where γ represents possible phase changes from the scattering process [Cumming and Wong, 2005].

As the SAR sensor moves along its path, FM pulses are transmitted coherently. Between transmitted pulses, the instrument 'listens' for echos from the point target. The total amount of time for the transmit and receive stages is called the pulse repetition interval (PRI), the inverse of which is the pulse repetition frequency (PRF). While the target remains within the beam footprint (as shown in Fig. 2.1), several pulses are backscattered at various energy levels to the SAR antenna. As the SAR instrument gets closer in slant-range to the point target, the received signal gets stronger and peaks at the beam center crossing time

$$\eta_c = -\frac{R_o\tan\theta_{sq}}{V_r}, \tag{2.7}$$

with θ_{sq} representing the squint angle. The middle plot of Fig. 2.2 illustrates the azimuth backscatter signal from the point target. Assuming an unweighted SAR antenna in the azimuth plane, the received signal $\omega_a(\eta)$ from the point target in the azimuth direction is approximately a squared sinc function centered about η_c. With this knowledge, we

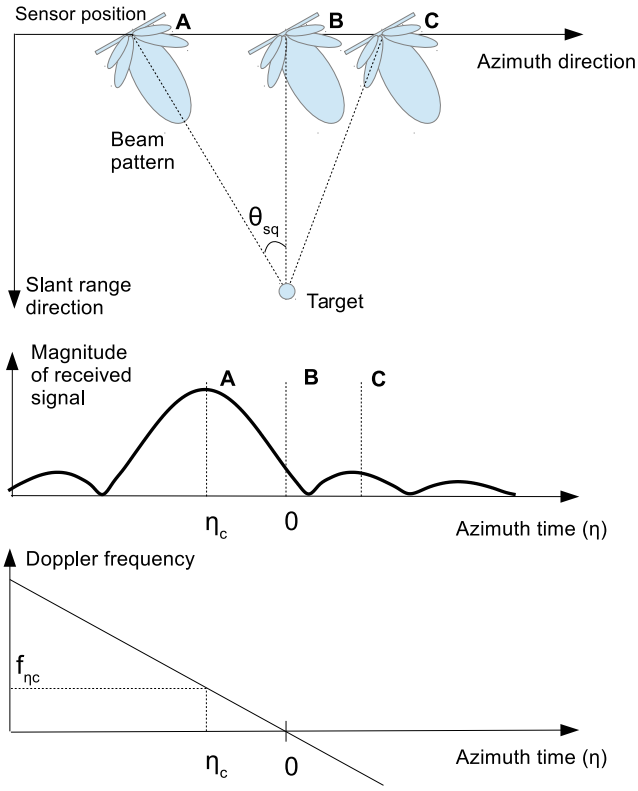

Figure 2.2: Plots showing the relationship between the sensor position, the magnitude of the received signal, and the Doppler frequency as the radar transmits its signal on a static target. The middle plot shows that the received signal is maximum when the target is in the radar line-of-sight at the beam center crossing time η_c. The Doppler frequency at η_c is referred to as the Doppler centroid (f_{η_c} or D_c). The bottom plot shows that the Doppler frequency varies linearly as the sensor moves forward and is zero at the time of closest approach (η=0).

are now ready to provide an expression for the real valued received SAR signal in both range and azimuth times

$$s_r(\tau,\eta) = A_t\omega_r(\tau - 2R(\eta)/c)\omega_a(\eta-\eta_c)\cos\left(2\pi f_o(\tau-2R(\eta)/c) + \pi K_r(\tau-2R(\eta)/c)^2+\gamma\right). \tag{2.8}$$

Note two additional variables included in (2.8) compared to (2.6), namely the azimuth two-way beam pattern ω_a and the change of R to $R(\eta)$ since the slant-range varies as the sensor moves. The received signal contains the radar carrier signal $\cos(2\pi f_o\tau)$ which can be removed using a quadrature demodulation process [Cumming and Wong, 2005] where we obtain the complex SAR signal

$$s_r(\tau,\eta) = A_t\omega_r(\tau - 2R(\eta)/c)\omega_a(\eta-\eta_c)e^{-j(4\pi f_o R(\eta)/c)}e^{j\pi(K_r(\tau-2R(\eta)/c)^2+\gamma)}. \tag{2.9}$$

A focused SAR image can be obtained by addressing the range and azimuth phase delays present in (2.9), respectively $2R(\eta)/c$ and η_c. A very common procedure in SAR focusing is to work in the Fourier domain and use carefully selected range and azimuth matched filters to compress the SAR data. A few well known SAR processing algorithms exist to accomplish such a task, namely

- the range Doppler algorithm (RDA)
- the chirp scaling algorithm (CSA)
- the Omega-K algorithm (ωKA)
- the SPECAN algorithm.

The reader is referred to appropriate textbooks such as [Cumming and Wong, 2005] and [Richards, 2005] for a detailed description of each of these algorithms and SAR theory, since it is out of the scope of this thesis.

The equivalent in the Fourier domain for the azimuth phase delay η_c is usually referred to as the Doppler centroid (f_{η_c}). This quantity can have an important role in SAR sea surface wind studies, which will be explored in section 2.2. For this reason, the following subsection provides further details about the Doppler centroid.

2.1.3 The Doppler centroid

By definition, the azimuth or Doppler frequency is proportional to the rate of change of the slant range with respect to azimuth time such that

$$f_\eta = -\frac{2}{\lambda}\frac{dR(\eta)}{d\eta}, \tag{2.10}$$

where $\lambda = c/f_o$ [Ulaby et al., 1981]. Using the range equation (see (2.1)), we find

$$\frac{dR(\eta)}{d\eta} = \frac{\eta V_r^2}{R(\eta)}. \tag{2.11}$$

This equation shows that the Doppler frequency varies linearly as a function of azimuth time, and is zero at $\eta = 0$ when the slant range $R(\eta)$=R_o (see top and bottom plots of Fig. 2.2).

As previously mentioned, matched filtering is a common technique used for SAR data compression in azimuth. Such a method requires the knowledge of the Doppler frequency at the beam center crossing time η_c where the target backscatter energy is maximum (corresponding to position A as shown on Fig. 2.2). This Doppler frequency is referred to as the Doppler centroid (f_{η_c} or D_c) such that

$$D_c = -\frac{2}{\lambda}\frac{\eta_c V_r^2}{R(\eta_c)} = \frac{2V_s \sin\theta_{sq,c}}{\lambda}, \tag{2.12}$$

where V_s is the satellite inertial velocity, and $\theta_{sq,c}$ is the squint angle at the beam center crossing time [Cumming and Wong, 2005]. Equation 2.12 is usually referred to as the geometric D_c since it is strictly a function of radar related parameters. Note that (2.12) is certainly valid when a SAR signal is reflected from a static target. In the case of a moving target such as the ocean surface however, the sea surface line-of-sight velocity must be determined in order to find the total D_c, as (2.12) does not account for the sea surface motion. In the next section, general sea surface wind retrieval procedures using active microwave sensors are discussed. A method including the D_c as a valid metric for sea surface wind retrieval is also presented.

2.2 Sea surface wind field retrieval

In this section, basic principles relating to sea surface scattering are discussed where the normalized radar cross section (NRCS) metric is defined. Common ocean wind retrieval processes employing such a metric are briefly mentioned. Finally, the potential of using the Doppler centroid from SAR in sea surface wind retrieval methods is discussed.

2.2.1 Sea surface scattering

One of the most basic relationships in the field of radar remote sensing (for monostatic radars) is the radar equation

$$P_r = \frac{\lambda_r^2}{(4\pi)^3} \int_A \frac{P_t G^2 \sigma^o dA}{R^4}, \tag{2.13}$$

where P_r is the received power, λ_r is the carrier wavelength, P_t is the transmitted power, G is the antenna gain, R is the distance between the illuminated area and the radar antenna, σ^o is the normalized radar cross section, and A is the illuminated area [Ulaby et al., 1981]. This equation provides a relationship between easily retrievable radar signal parameters and the normalized radar cross section (NRCS). The NRCS is in fact an important scattering parameter since it is characteristic of the target's size, material, shape, directivity, and orientation. In terms of electric fields, the NRCS can be expressed as

$$\sigma^o = \frac{4\pi R^2 |E_q^s|^2}{A|E_p^i|^2}, \tag{2.14}$$

where E_q^s represents the scattered electric field at polarization q, and E_p^i represents the incident electric field at polarization p [Ulaby et al., 1982]. In the context of radar remote sensing of the ocean surface, tiny capillary and short gravity waves induced by local wind stress (see Fig. 2.3) are the primary radar backscattering source such that

$$\lambda_s = \frac{\lambda_r}{2\sin\theta_i}, \tag{2.15}$$

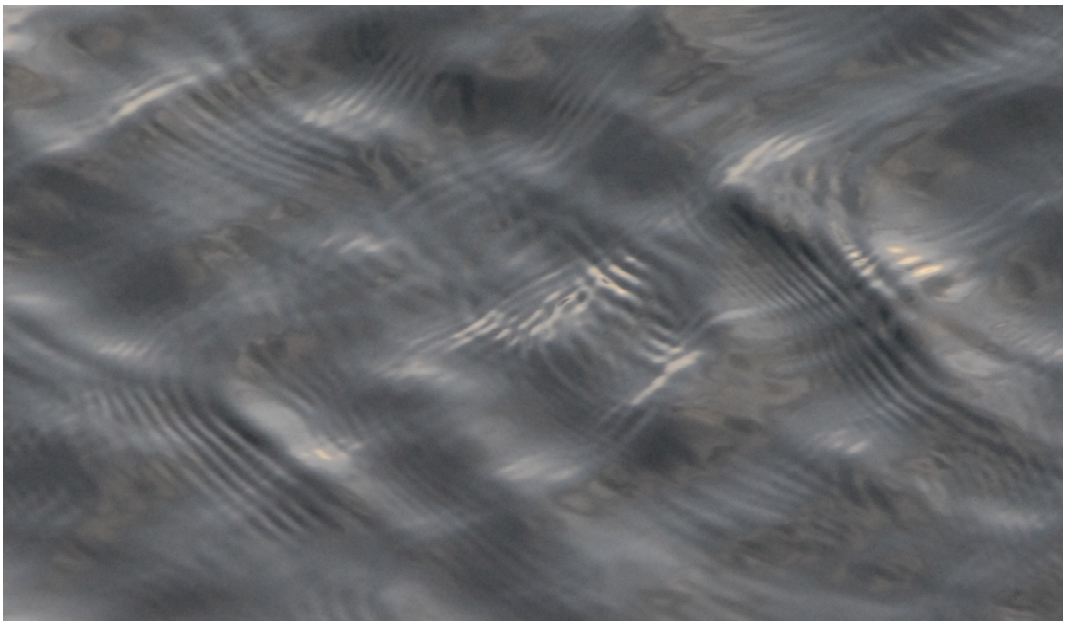

Figure 2.3: Snapshot of Bragg-scale waves present on the ocean surface generated by a wind blowing from the east (relative to the snapshot orientation).

where λ_s is the short Bragg-scale waves wavelength, and θ_i is the radar incidence angle [Ulaby et al., 1982]. As (2.15) shows, both the radar incidence angle and its operating frequency dictate the size of the detected surface waves.

Although the radar cannot directly detect waves with much longer wavelengths, their interaction with the shorter Bragg-scale waves within the illuminated area may still be noticeable. This is especially true when high resolution radars, such as SAR, are used to measure the ocean backscatter. Three primary mechanisms can be noted, namely hydrodynamic, tilt, and velocity bunching:

- the hydrodynamic effect refers to a change in the short waves shape and distribution due to the varying orbital velocities of water particles along the long waves surface (see Fig. 2.4)

- the tilt modulation is due to the varying slopes of the long waves affecting the local orientation of the short waves with respect to the radar look angle. As a result, the backscatter signal from the short waves is altered from these slopes

- when long waves are traveling perpendicular to the radar look direction, the radial orbital velocity from the water particles cannot be detected by the radar. This results in an apparent increase or decrease in the density of scatters in the azimuth direction on the SAR image. This effect is referred to as velocity bunching [Alpers and Rufenach, 1979].

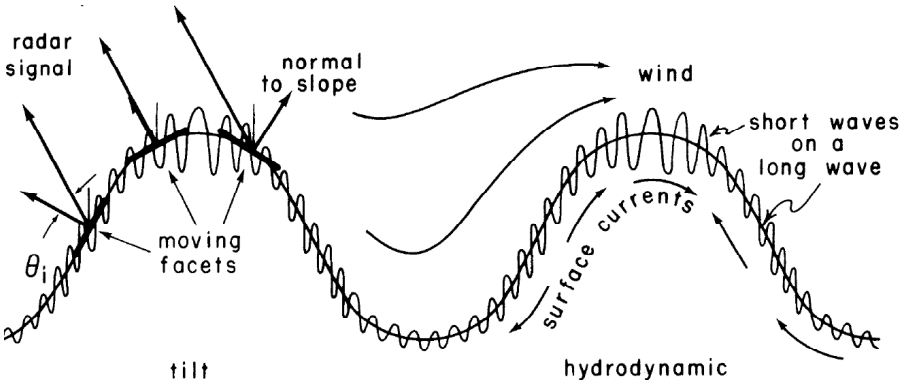

Figure 2.4: In this illustration, a short wave is riding on a long wave. The orbital velocity of the water particles along the sea surface is affected by the long wave, which in turn modulates the shape and distribution of the short wave. This phenomenon is referred to as the hydrodynamic modulation (courtesy of [Stewart, 1985]).

It is important to note that if one's goal is to estimate the wind field from a SAR intensity image, the latter mechanism can be neglected to a certain extent since the wind field is estimated by averaging the backscatter signal over a given area. Velocity bunching must be taken into consideration however, if ocean wave spectra estimation is desired. Other geophysical phenomena such as sea surface currents, wave breaking, the presence of cloud, rain, snow, or ice can also influence the radar backscatter signal. Depending on the instrument's carrier frequency, polarization state, and viewing angle, some of these effects can either be negligible or of great importance [Ulaby et al., 1981].

It is possible to simulate the NRCS by using a model for the scattered electric field in (2.14), or its equivalent magnetic field. Two of the most common scattering models are the Kirchhoff approximation (KA) [Beckmann and Spizzichino, 1963] and the small perturbation method (SPM) [Ulaby et al., 1982]. The KA model yields the following scattered magnetic field at the field point R over a flat reference plane A [Elfouhaily et al., 1999]:

$$\mathbf{B}_s(R) = -\frac{\imath}{2\pi}\frac{e^{\imath kR}}{R} B_0 k \mathbf{P}_s \int_A d\mathbf{x} e^{-\imath(Q_z \eta(\mathbf{x}) + \mathbf{Q}_h \cdot \mathbf{x})}, \tag{2.16}$$

where $k = |\mathbf{k}|$ is the electromagnetic wavenumber ($\mathbf{k} = (\mathbf{k}_h, k_z)$), B_0 is the magnitude of the incident magnetic field, $\eta(\mathbf{x})$ represents the sea surface elevation, $\mathbf{Q}_r$ is the Ewald vector with components $Q_z = k_z^s - k_z^i$, $\mathbf{Q}_h = \mathbf{k}_h^s - \mathbf{k}_h^i$ (superscripts i and s refer to incident and scattered, respectively), and the scattered polarization vector is

$$\mathbf{P}_s = [\tfrac{\mathbf{Q}_r}{Q_z} \times \hat{P}_i^p] \times \tfrac{\mathbf{R}}{R},$$

with $\hat{P}_i^p$ being the incident polarization vector with polarization p. While the scattering model based on KA is valid for small and long wavelengths, it lacks polarization sensitivity.

An improvement to (2.16) is made by Elfouhaily *et al.* [Elfouhaily et al., 1999] [Elfouhaily et al., 2001] where the polarization sensitivity issue is in fact addressed. The resulting scattered magnetic field yields the same expression as (2.16), but with the following scattered polarization vector

$$\mathbf{P}_s = \left\{ 2(\tfrac{\mathbf{Q}_h}{Q_z} \cdot \mathbf{P}_h)\mathbf{Q}_h - (\tfrac{\mathbf{Q}_h}{Q_z} \cdot \mathbf{Q}_h)\mathbf{P}_h \right\} \times \tfrac{\mathbf{R}}{R},$$

where $\mathbf{Q}_h = \frac{1}{2}(\frac{\mathbf{k}_h^s}{k_z^s} + \frac{\mathbf{k}_h^i}{k})$, and $\mathbf{P}_h = \hat{e}_z \times \hat{P}_i^p$. The scattered magnetic field related to the SPM can be found by expanding the phase factor of (2.16) as described in [Christopher R. Jackson, 2004b]:

$$\mathbf{B}_s(R) = -\frac{\imath}{2\pi}\frac{e^{\imath kR}}{R} B_0 k \mathbf{P}_s \int_A d\mathbf{x}(1 - \imath Q_z \eta(\mathbf{x}))e^{-\imath \mathbf{Q}_h \cdot \mathbf{x}}. \tag{2.17}$$

The SPM also yields proper polarization sensitivity over the KA model, though the former model is only valid for small slopes and short wavelengths.

Regardless of the selected scattering model, the NRCS can then be computed with a relation based on 2.14 where

$$\sigma_{pq}^o = \lim_{R\to\infty} \frac{4\pi R^2}{A} \frac{\langle \mathbf{B}_s(R)\mathbf{B}_s^*(R)\rangle}{B_0^2}, \tag{2.18}$$

with $\langle\rangle$ being the ensemble average operator, and pq referring to incident and scattered polarizations, respectively. In the following subsection, we discuss the various methods used to infer the ocean surface wind fields from measured σ^o.

2.2.2 Common wind retrieval methods

Radars such as scatterometers or SAR can be used to infer the wind field from ocean backscatter measurements. Scatterometers have the advantage of providing large spatial coverage with high repeat rate compared to SAR instruments. The latter, however, provide much finer resolution products compared to scatterometers. In fact, SAR instruments are the preferred tool of choice for submesoscale ocean feature detection such as eddies, fronts, filaments, and spirals [Chapron et al., 2005] [Kudryavtsev et al., 2005] [Johannessen et al., 2005]. Furthermore, they are less prone to land contamination, and can be used to detect ocean winds in coastal areas.

Regardless of the radar instrument used, the local wind field cannot be directly extracted from ocean backscatter measurements. A common method to infer the sea surface wind information from radar measurements relies on the use of semi-empirical geophysical model functions (GMFs). These functions commonly relate the NRCS with geophysical and radar parameters such that

$$\sigma^o = G(u_{10}, \phi, f, pol, \theta_i), \tag{2.19}$$

Table 2.1: List of previously launched scatterometers including the corresponding GMF used for ocean wind retrieval purposes

Scatterometer	launch date	frequency band	GMF used
Seasat	27 Jun 1978	Ku-band	SASS-2 [Wentz et al., 1984]
ERS-1	17 Jul 1991	C-band	CMOD3 [Long, 1995]
ERS-2	21 Apr 1995	C-band	CMOD2-I3 [Bentamy et al., 1999]
NSCAT	16 Aug 1996	Ku-band	NSCAT-1 [Wentz and Smith, 1999]
QuikSCAT	19 Jun 1999	Ku-band	QSCAT-1/F13 [Lungu, 2006]
ASCAT	19 Oct 2006	C-band	CMOD5.n [Hersbach, 2010]
OSCAT	23 Sep 2009	Ku-band	TNNL_OCT [Gohil et al., 2013]

where u_{10} is the wind speed at a height of 10 meters, ϕ is the wind direction relative to the range direction, f is the radar operating frequency, pol is the polarization state, and θ_i is the local incidence angle. Almost all GMFs are semi-empirical and are commonly tailored to work optimally at a given polarization state (usually VV) and frequency. If it is desired to use a given GMF at a different polarization (e.g. HH), a conversion process can be used such that

$$\sigma^o_{HH} = \sigma^o_{VV\,gmf} \cdot \left(\frac{\sigma^o_{HH}}{\sigma^o_{VV}} \right)_{mod}, \tag{2.20}$$

where $\sigma^o_{VV\,gmf}$ are the modeled backscatter values from the GMF at VV polarization, and $(\frac{\sigma^o_{HH}}{\sigma^o_{VV}})_{mod}$ represents a modeled polarization ratio [Mouche et al., 2005] [Johnsen et al., 2008].

Table 2.1 provides a list of well known GMFs used with specific scatterometers. Although each of these GMFs are designed to work with a specific radar instrument, a general relationship can be written between the measured σ^o and geophysical and radar parameters

$$\sigma^o = B_0[1 + B_1 \cos(\phi) + B_2 \cos(2\phi)]^z, \tag{2.21}$$

where ϕ is the wind direction relative to the range direction, the coefficients B_0, B_1, and B_2 are related to the wind speed, incidence angle, polarization state, radar frequency, and the exponent z is a tuning parameter [Jones et al., 1977] [Wentz et al., 1984]. Using the CMOD5.n GMF, Fig. 2.5 shows the relationship between the radar backscatter and the wind direction given a 10 m/s wind speed and 22, 30, 38 degree incidence angles. From this figure we note that

- σ^o decreases as the incidence angle increases given a fixed wind speed, wind direction, and polarization state
- σ^o peaks in up and down-wind conditions, with the former being the global maximum when the incidence angle is greater than $\sim$25 degrees
- given a polarization state and incidence angle, a single σ^o measurement leads to multiple wind solutions (usually referred to as ambiguities).

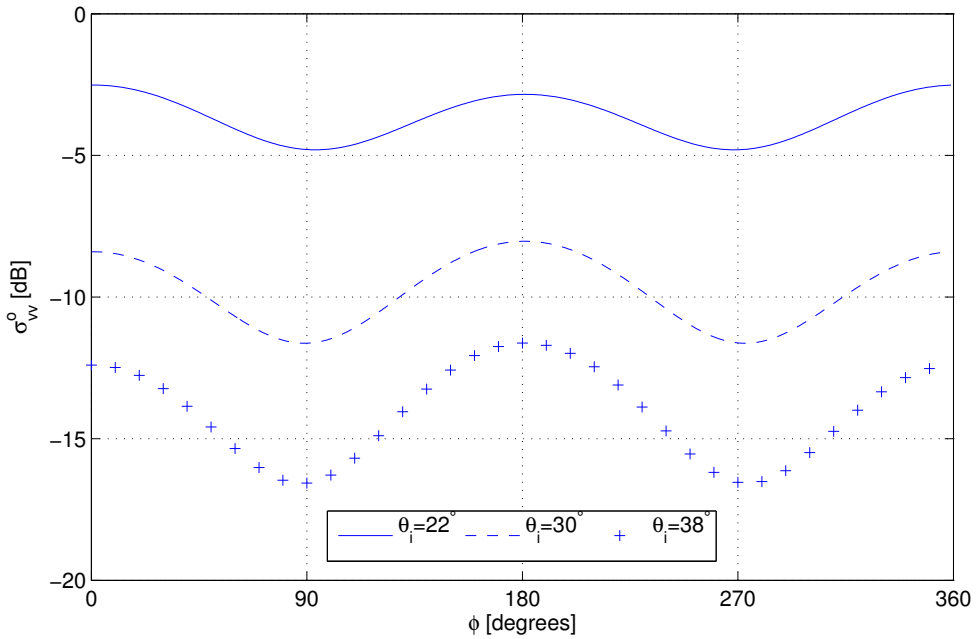

Figure 2.5: Plot of the normalized radar cross section in terms of the wind direction at VV polarization given u_{10}=10 m/s and three incidence angles using the CMOD5.n GMF. For a given incidence angle, σ^o is maximum at up-wind except when $\theta_i < 25^o$. σ^0 also decreases as the incidence angle increases. Several wind solutions are possible for a given σ^o measurement. In this figure, down-wind corresponds to $\phi = 0$.

The latter observation complicates the wind inversion process from measured radar backscatter, and requires the use of methods based on estimation theory. As an illustration, the wind inversion process from QuikSCAT backscatter measurements is based on the use of a maximum-likelihood estimator (MLE) with the objective function

$$J = -\left[\sum_{i=1}^{N} \frac{(\sigma^o_{mes} - \sigma^o_{mod}(u_{10}, \phi_i))^2}{Var(\sigma^o_{mod})_i} + \ln(Var(\sigma^o_{mod})_i)\right] \tag{2.22}$$

where σ^o_{mes} are the backscatter measurements, σ^o_{mod} are the corresponding model backscatter values and $Var(\sigma^o_{mod})_i$ are the measurements variances [Lungu, 2006]. Similarly, sea surface wind retrieval using the ASCAT radar instrument requires minimizing

$$J = (z_{meas} - z_{mod}(u_{10}, \phi_i))^2, \tag{2.23}$$

where $z = (\sigma^o)^{0.625}$ are modified σ^o value, z_{meas} corresponds to equivalent measured backscatter data, and z_{mod} corresponds to modeled backscatter value [Ocean and SAF, 2011]. An ambiguity removal process is required as the above estimators still lead to a set of multiple wind solutions. The number of solutions in the set depends on the instrument used, where its scanning method is the main factor; in the case of QuikSCAT,

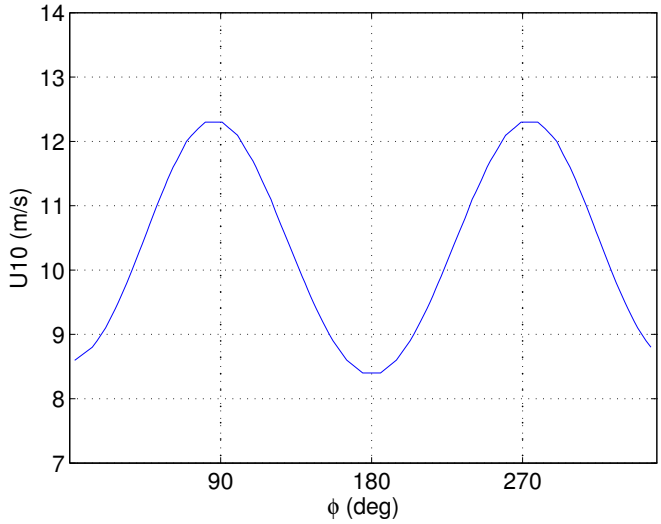

Figure 2.6: Plot showing the set of wind solutions for a -7.86 dB σ^o_{vv} measurement at a 28.8 degree incidence angle at X-band. Though the range of possible wind speeds is measurable (i.e. $\sim$8.75-12.25m/s), the wind direction component is completely unknown.

the number of ambiguity usually ranges from two to six [Lungu, 2006], whereas for ASCAT there can be up to four ambiguities [Ocean and SAF, 2011].

The problem becomes much more complicated when using SAR stripmap σ^o data. Due to a single viewing angle, a single σ^o measurement is retrieved per wind vector cell which leads to a large number of wind solutions. If SAR sea surface wind retrieval is desired, either ancillary data or other radar measurements must be used to help solving for the true wind. In the following subsection, the Doppler centroid is considered as an additional parameter to backscatter measurements, to make sea surface wind retrieval possible from SAR.

2.2.3 The combined use of NRCS and Doppler centroid

SAR stripmap NRCS measurements alone are insufficient to successfully retrieve the wind information. Using dual-polarized stripmap TerraSAR-X data, Fig. 2.6 shows the multiple wind solutions corresponding to a -7.96 dB σ^o_{vv} measurement with a 28.8 degree incidence angle at X-band. Though such a measurement provides a quantifiable range of wind speeds (i.e. $\sim$ 8.75-12.25 m/s), the true wind direction cannot be solved using SAR NRCS measurements alone. This issue can be alleviated with the use of ancillary data, such as numerical weather prediction models or in-proximity *in situ* weather data, providing *a priori* information regarding the wind direction [Wackerman et al., 1996] [Bergeron et al., 2011].

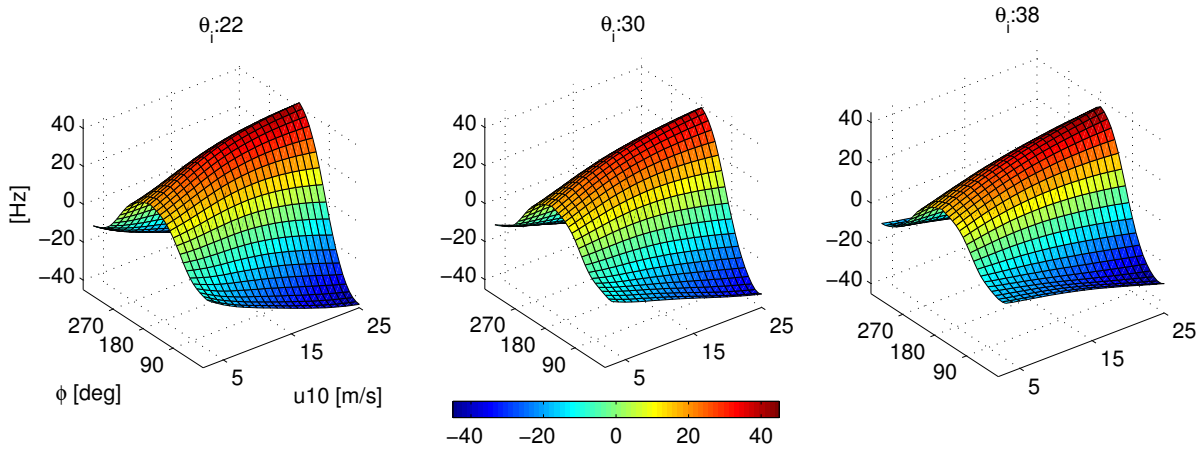

Figure 2.7: 3D plots of the D_c in terms of the wind field given three incidence angles. These simulation plots have been done using the CDOP GMF [Mouche et al., 2012].

If such a dataset is not available, SAR wind streak detection methods can be used as an alternative to provide the wind direction information [Horstmann and Koch, 2005]. Though effective, this method is limited to high wind speed cases since wind streaks can only be detected in such situations.

An alternative method exists where the Doppler centroid (D_c) is used as an additional SAR parameter along with the NRCS to infer the sea surface wind field. In fact, Mouche *et al.* [Mouche et al., 2012] shows that the use of the Doppler centroid anomaly (i.e. the difference between the geometric D_c as in (2.12), and the measured D_c) combined with C-band NRCS measurements at the VV polarization, can improve wind direction retrieval. Such a method requires the use of a specific geophysical model function which relates the D_c contribution from local wind stress with the sea surface wind. In [Mouche et al., 2012], the CDOP GMF is used to retrieve the wind from C-band SAR Doppler measurements. Figure 2.7 shows how the D_{cVV} from the CDOP GMF varies in terms of the relative wind direction given three different incidence angles. There are several important characteristics to note from this figure pertaining to the D_c:

- the D_c extrema always occur both in up- and down-wind conditions
- the D_c monotonically varies between up- and down-wind
- it is always greater (in absolute value) in up-wind compared to down-wind
- given any wind direction and incidence angle, the D_c increases in terms of wind speed
- given any wind speed and direction, the D_c decreases with an increasing incidence angle

- there are always two possible D_c values associated to a given wind speed and incidence angle, ultimately leading to two possible wind directions
- the sign of the D_c dictates either an up- or down-wind condition; in our convention, a positive D_c leads to an up-wind condition.

If one includes the D_c as an additional metric in the wind retrieval process, a method based on a maximum a posteriori estimator can be used where the following cost function is minimized

$$J = \frac{(\sigma_m^o - \sigma_{GMF}^o(\mathbf{u}))^2}{Var(\sigma_m^o)} + \frac{(D_{cm} - D_{cGMF}(\mathbf{u}))^2}{Var(D_{cm})} + \frac{(\mathbf{u} - \mathbf{u}_B)^2}{Var(\mathbf{u})}. \tag{2.24}$$

In the above equation, σ_m^o and D_{cm} are measured quantities, σ_{GMF}^o and D_{cGMF} are the NRCS and Doppler centroids from their respective model functions, and the last ratio corresponds to a selected prior where $\mathbf{u_B}$ is an *a priori* wind vector [Mouche et al., 2012]. Though effective, using single polarized D_c measurements may contain both wind and surface current induced radial velocities. In chapter 3, we explore a very similar method at X-band using dual-polarized data. Specifically, the metrics used for the wind inversion are the backscatter measurements and the polarization residual Doppler frequency ($D_{cVV} - D_{cHH}$). Using the Doppler centroid difference should eliminate the majority of the radial velocity induced by possible sea surface current [Romeiser and Thompson, 2000]. Since the work presented in chapter 3 has been done at X-band, alternative backscatter and Doppler centroid GMFs are implemented. The next section provides further details regarding these theoretical GMFs.

2.3 GMFs based on the generalized ocean surface curvature model

[Engen et al., 2006] developed an electromagnetic scattering model, called the generalized curvature ocean surface scattering model (GCM), where both SPM and KA results as well as fundamental laws of reciprocity and tilt invariance are preserved up to first order. Given specific geophysical and radar parameters, both the normalized radar cross section and the Doppler centroid can be theoretically derived using the GCM. In this section, we provide a high level derivation of both the backscatter and D_c models based on this electromagnetic scattering model.

2.3.1 Backscatter model

Similar to 2.18, the NRCS can be expressed as

$$\sigma^o = \lim_{R\to\infty} \frac{4\pi R^2}{|A|} \left\langle \left| \frac{\hat{\mathbf{B}}_s \cdot \mathbf{B}(\mathbf{R})}{|\mathbf{B}_i|} \right|^2 \right\rangle, \tag{2.25}$$

where $\hat{\mathbf{B}}_s$ represents the polarization state of the scattered magnetic field, $\mathbf{B}(\mathbf{R})$ is the total magnetic field at the position $\mathbf{R}$ at the center of the illuminated area A, $\mathbf{B}_i$ represents the incident magnetic field, and $\langle\cdot\rangle$ is the ensemble average operator. The ratio in (2.25) can be expressed as

$$\frac{\hat{\mathbf{B}}_s \cdot \mathbf{B}(\mathbf{R})}{|\mathbf{B}_i|} = \frac{\imath k_r}{4\pi R} \int_A d\mathbf{x} e^{-\imath(\mathbf{Q}_h \cdot \mathbf{x} + Q_z \eta(\mathbf{x}))} F(\mathbf{x}), \tag{2.26}$$

where k_r is the magnitude of the radar wave vector $\mathbf{k}_r$, $\eta(\mathbf{x})$ is the surface elevation, and $F(\mathbf{x})$ represents a source function caused by the electric surface current as defined by [Engen et al., 2006] such that

$$F(\mathbf{x}) \approx F^{(0)} + F^{(1)}(\mathbf{x}), \tag{2.27}$$

where the exponents refer to the order. Expressions for both $F^{(0)}$ and $F^{(1)}(\mathbf{x})$ are provided in chapter 4.

Assuming statistical stationarity, (2.25) becomes

$$\sigma^o = \frac{k_r^2}{4\pi} \int d\mathbf{x} e^{-\imath \mathbf{Q}_h \cdot \mathbf{x}} \langle e^{-\imath Q_z(\eta(\mathbf{x}) - \eta(\mathbf{0}))} F(\mathbf{x}) F^*(\mathbf{0}) \rangle. \tag{2.28}$$

In order to provide a backscatter model, a solution for the Fourier kernel in (2.28) must be found where expressions for both the sea surface elevation and source function are needed. Considering a monochromatic surface wave, the Airy wave theory provides a linear description of surface gravity wave propagation along the sea surface [Airy, 1841] where the sea surface elevation η is described such that

$$\tilde{x} = x, \tag{2.29}$$

$$\eta = a\cos(kx - wt). \tag{2.30}$$

In this set of equations, x is a reference point at the sea surface, a represents the wave amplitude, k the wave number, and w the angular frequency. Such a description of wave propagation along the sea surface is referred to as Eulerian. Although very simple to implement due to its linearity, it only describes sinusoidal wave profiles. A slightly more realistic wave description can be accomplished by including a shifting term in the horizontal coordinate where

$$\tilde{x} = x - a\sin(kx - wt) \tag{2.31}$$

$$\eta = a\cos(kx - wt). \tag{2.32}$$

Such a change of coordinate system is referred to as a Lagrangian description of fluid motion, which includes Stokes-like waves with sharper crests and wider troughs as shown in Fig. 2.8. Implementing this additional horizontal shift from (2.31) in (2.28)

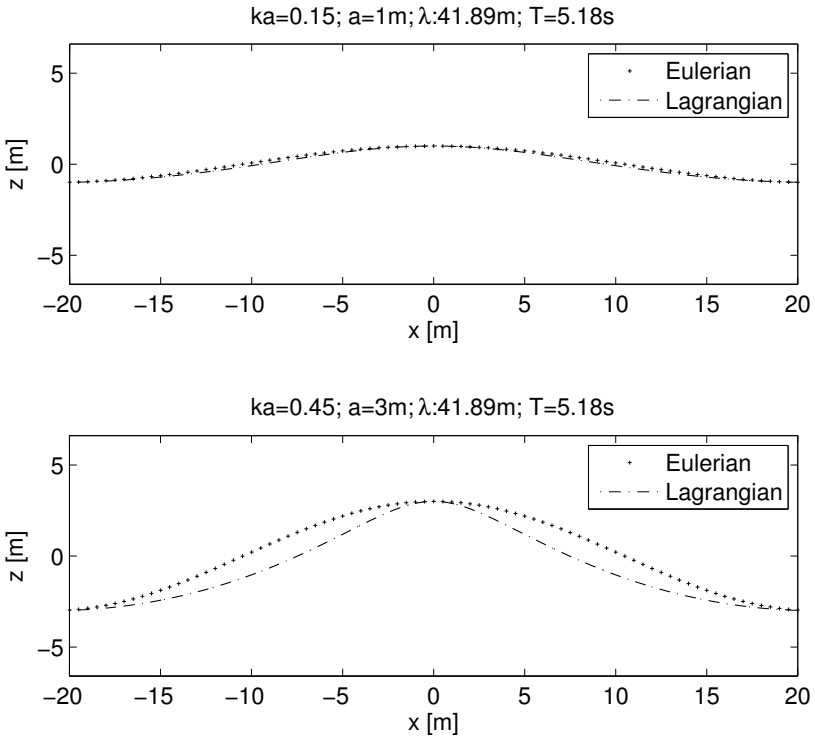

Figure 2.8: A Eulerian vs. a Lagrangian representations of a surface wave. In the upper plot, the wave amplitude is 1m vs. 3m on the bottom plot. All other variables are kept the same. In the upper plot, the Lagrangian representation of the ocean wave is very similar to the Eulerian one. As the amplitude grows, the former provides a more realistic wave description with a sharper crest and a wider trough.

leads to

$$\sigma^o = \frac{k_r^2}{4\pi} \int d\mathbf{x} e^{-\imath \mathbf{Q}_h \cdot \mathbf{x}} \langle e^{-\imath \mathbf{Q}_r \cdot (\boldsymbol{\chi}(\mathbf{x}) - \boldsymbol{\chi}(\mathbf{0}))} F(\mathbf{x}) J(\mathbf{x}) F^*(\mathbf{0}) J^*(\mathbf{0}) \rangle, \tag{2.33}$$

with $\boldsymbol{\chi}$ describing the orbital motion of a fluid particle with components $(\boldsymbol{\xi}, \eta)$. The Jacobian $J(\mathbf{x})$ in (2.33) is defined up to first order

$$J(\mathbf{x}) = \det \begin{bmatrix} 1 + \frac{\partial \xi_x}{\partial x} & \frac{\partial \xi_y}{\partial x} \\ \frac{\partial \xi_x}{\partial y} & 1 + \frac{\partial \xi_y}{\partial y} \end{bmatrix} \approx 1 + \nabla \cdot \boldsymbol{\xi}. \tag{2.34}$$

In (2.33), we can then rewrite

$$F(\mathbf{x}) J(\mathbf{x}) F^*(\mathbf{0}) J^*(\mathbf{0}) = f(\mathbf{x}) f^*(\mathbf{0}), \tag{2.35}$$

where

$$f(\mathbf{x}) = \underbrace{F^{(0)}}_{f^{(0)}} + \underbrace{(F^{(0)} \nabla \cdot \boldsymbol{\xi} + F^{(1)}(\mathbf{x}))}_{f^{(1)}}. \tag{2.36}$$

Using the relation

$$e^{\imath X}Y = -\imath \left\{ \frac{\partial e^{\imath(X+\lambda Y)}}{\partial \lambda} \right\}_{\lambda=0}, \tag{2.37}$$

and assuming that the variables $\boldsymbol{\chi}$ and $f(\mathbf{x})$ are Gaussian, the Fourier kernel in (2.33) becomes

$$\begin{aligned}\langle e^{-\imath(\zeta(\mathbf{x})-\zeta(\mathbf{0}))} f(\mathbf{x}) f^*(\mathbf{0})\rangle = e^{\varphi_{\zeta\zeta}(\mathbf{x})-\varphi_{\zeta\zeta}(\mathbf{0})} \\ [\varphi_{f^{(1)}f^{(1)}}(\mathbf{x}) + (f^{(0)} + \imath(\varphi_{f^{(1)}\zeta}(\mathbf{x}) - \varphi_{f^{(1)}\zeta}(\mathbf{0}))) \\ (f^{*(\mathbf{0})} - \imath(\varphi_{\zeta f^{(1)}}(\mathbf{x}) - \varphi_{\zeta f^{(1)}}(\mathbf{0})))],\end{aligned} \tag{2.38}$$

where $\zeta = \mathbf{Q}_r \cdot \boldsymbol{\chi}$, and all φ_{ab} represent covariance functions. By definition, the covariances in (2.38) can be computed such that

$$\varphi_{ab}(\mathbf{x}) = \langle (a(\mathbf{x}) - \langle a\rangle)(b(\mathbf{x}) - \langle b\rangle)^*\rangle. \tag{2.39}$$

For ease of implementation, it may be more convenient to compute these covariances in the $\mathbf{k}$ domain. Equation (2.39) then becomes

$$\varphi_{ab}(\mathbf{x}) = Re\left\{ \frac{1}{(2\pi)^2} \int d\mathbf{k} e^{\imath(\mathbf{k}\cdot\mathbf{x})} T_a(\mathbf{k}) T_b{}^*(\mathbf{k}) \Gamma(\mathbf{k}) \right\}, \tag{2.40}$$

where $T_a(\mathbf{k})$ and $T_b(\mathbf{k})$ are transfer functions, and $\Gamma(\mathbf{k})$ is the power spectral density of the sea surface elevation, or most commonly known as the surface wave spectrum [Engen et al., 2000]. The needed transfer functions are then

$$T_\zeta = \mathbf{Q}_r \cdot T_{\boldsymbol{\chi}}, \tag{2.41}$$

$$T_{f^{(1)}} = F^{(0)} T_J + T_{F^{(1)}(\mathbf{x})}, \tag{2.42}$$

where $T_{\boldsymbol{\chi}}$ and T_J can be found using the first order Lagrangian formulation of Bernoulli's law, which is described below (see [Engen et al., 2006] for a detailed derivation of $T_{F^{(1)}(\mathbf{x})}$).

In the (common) Eulerian frame of reference, Bernoulli's equation for incompressible fluids is

$$\frac{\partial \phi}{\partial t} + \frac{1}{2}|\nabla\phi|^2 + g\eta - \underbrace{\frac{T}{\rho}\left(\frac{\partial^2 \eta}{\partial x^2} + \frac{\partial^2 \eta}{\partial y^2}\right)}_{-P/\rho} = 0\,, \qquad z = \eta \tag{2.43}$$

where $\phi(\mathbf{r}, t)$ represents the velocity potential, g is the standard acceleration due to gravity, T is the surface tension coefficient, ρ is the fluid density, P the fluid pressure, z is the component of the vertical axis. In order to obtain the equivalent Lagrangian formulation of (2.43), a set of differential operators are required based on

$$\tilde{\mathbf{r}} = \mathbf{r} + \boldsymbol{\chi}(\mathbf{r}, t)\,, \qquad \tilde{t} = t, \tag{2.44}$$

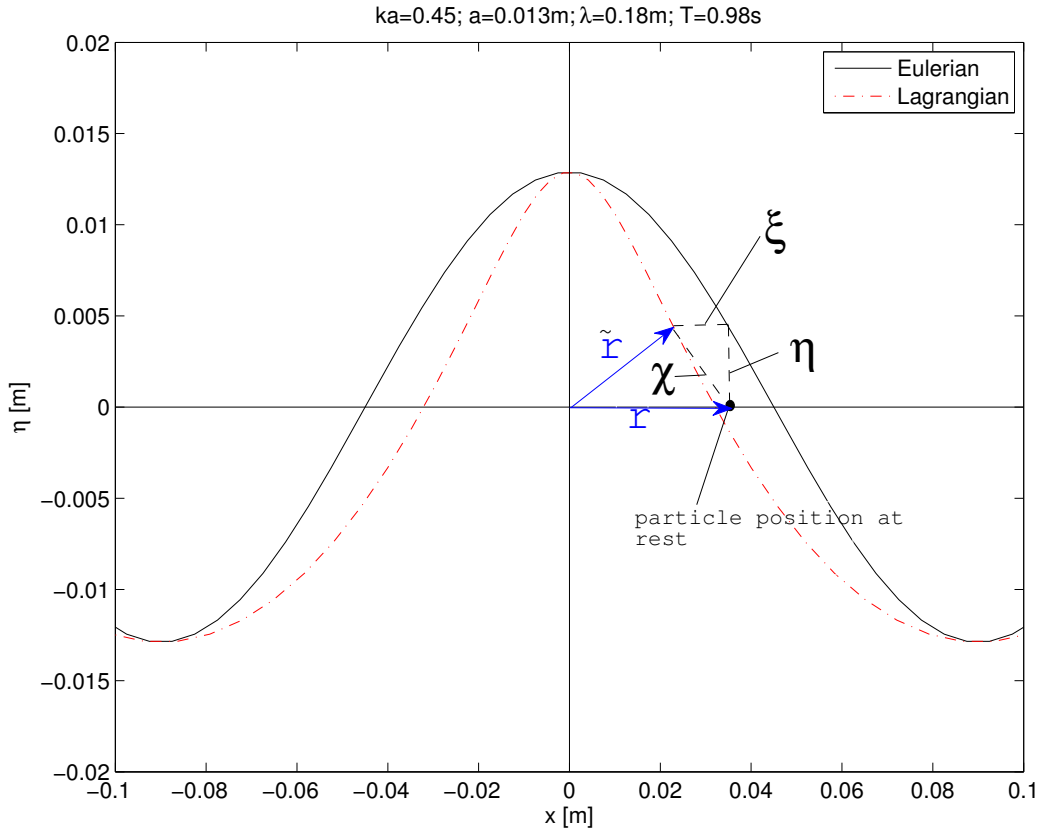

Figure 2.9: Plot of a Lagrangian and a Eulerian surface waves. The vector $\mathbf{r}$ refers to the reference position a fluid particle at rest, while the vector $\tilde{\mathbf{r}}$ refers to the position of that same fluid particle moving on a Lagrangian surface. $\boldsymbol{\chi}(\xi, \eta)$ describes the orbital motion of the particle.

where $\tilde{\mathbf{r}}(\tilde{\mathbf{x}}, \eta)$ refers to the position of a fluid particle moving around a Lagrangian reference position $(\mathbf{r}, t)$, and $\boldsymbol{\chi}$ describing its orbital motion (see Fig. 2.9). These differential operators are

$$\frac{\partial}{\partial \tilde{t}} = \frac{\partial}{\partial t} - \frac{\partial \boldsymbol{\chi}}{\partial t} \cdot \nabla' \tag{2.45}$$

$$\frac{\partial}{\partial \tilde{r}_j} = \frac{\partial}{\partial r_j} - \frac{\partial \boldsymbol{\chi}}{\partial r_j} \cdot \nabla' \tag{2.46}$$

$$\tag{2.47}$$

with

$$\nabla' = \frac{1}{1 + \nabla \boldsymbol{\chi}} \cdot \nabla = \sum_{n=0}^{\infty} (-\nabla \boldsymbol{\chi})^n \cdot \nabla \, . \tag{2.48}$$

Bernoulli's law then becomes

$$\frac{\partial \phi}{\partial \tilde{t}} - \frac{1}{2}\left|\frac{\partial \boldsymbol{\chi}}{\partial \tilde{t}}\right|^2 + g\eta - B = 0\,, \quad z = 0 \tag{2.49}$$

where $B = \frac{T}{\rho}\left[\left(\frac{\partial^2 \eta}{\partial x^2} - \frac{\partial \boldsymbol{\chi}}{\partial x}\cdot\nabla'\eta\right) + \left(\frac{\partial^2 \eta}{\partial y^2} - \frac{\partial \boldsymbol{\chi}}{\partial y}\cdot\nabla'\eta\right)\right]$.

To first order, (2.49) simplifies to

$$\frac{\partial \phi^{(1)}}{\partial \tilde{t}} + g\eta^{(1)} - \frac{T}{\rho}\left(\frac{\partial^2 \eta^{(1)}}{\partial x^2} + \frac{\partial^2 \eta^{(1)}}{\partial y^2}\right) = 0\,, \quad z = 0. \tag{2.50}$$

We are now ready to derive the transfer functions described in (2.41) and (2.42). Beginning with (2.41), an expression for $T_{\boldsymbol{\chi}}$ is required. Since the particle velocity is related to the velocity potential

$$\frac{\partial \boldsymbol{\chi}}{\partial \tilde{t}} = \nabla \phi\,, \tag{2.51}$$

a solution for the velocity potential transfer function is required in order to find $T_{\boldsymbol{\chi}}$. Let

$$\phi^{(1)}(\tilde{\mathbf{r}}, \tilde{t}) = \iint d\mathbf{k} d\omega e^{i(\mathbf{k}\cdot\mathbf{x} - \omega t)}\, T_{\phi}^{(1)}(\mathbf{k}, \omega, z)\, \hat{\eta}(\mathbf{k}, \omega)\,, \tag{2.52}$$

where $\hat{\eta}$ is the Fourier transform of the surface elevation, we can find $T_{\phi}^{(1)}$ using both (2.50) and the dispersion relation

$$\omega^2 \approx gk + \frac{T}{\rho}k^3. \tag{2.53}$$

This leads to

$$T_{\phi}^{(1)}(\mathbf{k}, \omega, z) = -i\,\frac{\omega}{k}\,\frac{\cosh\left[k(z+h)\right]}{\sinh(kh)}. \tag{2.54}$$

Using (2.54) combined with the relation from (2.51), the transfer function (to first order) for the variable $\boldsymbol{\chi}$ is

$$T_{\boldsymbol{\chi}}^{(1)}(\mathbf{k}, \omega, z) = \left(T_{\xi}^{(1)}, T_{\eta}^{(1)}\right) \approx \left(i\hat{\mathbf{k}}\frac{\cosh[k(z+h)]}{\sinh(kh)}\,, 1\right)\,, \tag{2.55}$$

yielding

$$T_{\zeta} = \mathbf{Q}_r \cdot T_{\boldsymbol{\chi}}^{(1)} = \imath \mathbf{Q}_h \cdot \hat{\mathbf{k}} + Q_z, \tag{2.56}$$

and

$$T_{f^{(1)}} = -kF^{(0)} + T_{F^{(1)}}(\mathbf{k}). \tag{2.57}$$

Figure 2.10 shows simulated HH and VV backscatter signals at C-band (f=5.4 GHz), given u_{10}=12 m/s, and three different incidence angles; the polarization ratio (i.e. $\sigma^o_{VV}/\sigma^o_{HH}$) is also provided. As expected, the σ^o_{VV} is greater than σ^o_{HH} for the selected incidence angles. Their ratio becomes larger as the incidence angle increases.

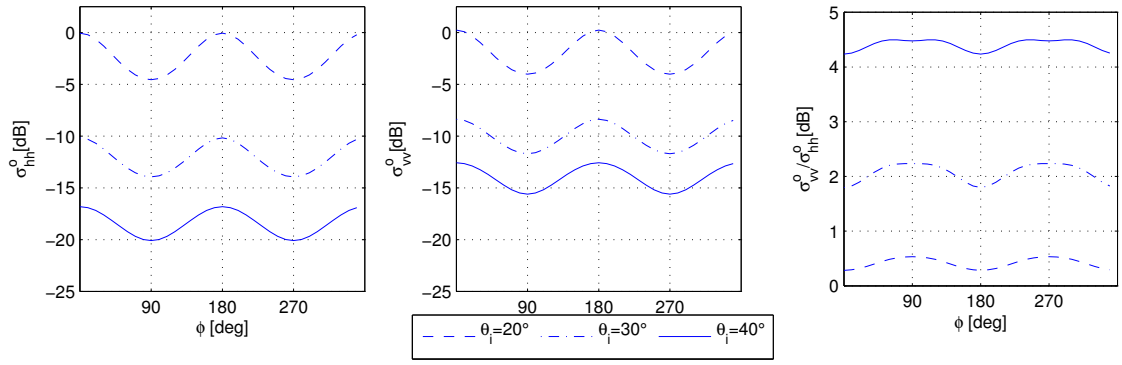

Figure 2.10: Simulated HH and VV backscatter signals based on the GCM for three incidence angles at C-band (f=5.4 GHz). Selected u_{10} is 12 m/s. The third plot represents the polarization ratio.

It is important to note that the above description of the GCM based backscatter model excludes breaking wave effects onto the NRCS. In [Johnsen et al., 2008], the inclusion of such effects based on [Kudryavtsev et al., 2003] is analyzed. In chapter 4, the impact of such a Lagrangian implementation in the GCM based backscatter model with a breaking wave component is compared with an empirical C-band GMF, and extended with a skewness parameter which provides a better description of the sea surface.

2.3.2 Doppler model

Using the generalized curvature model (GCM) [Engen et al., 2006], it is also possible to derive the Doppler centroid. This claim is based on the assumption that the D_c can be found using a spectral moment estimation method where the first order moment of the power spectral density (PSD) of the complex SAR image (normalized to the zeroth order moment) corresponds to the D_c. In this section, a high level description of the D_c derivation, based on [Pedersen et al., 2004], is provided beginning with an expression of the convolution of the transmitted SAR signal with the ocean surface reflectivity in ground-range coordinates $\mathbf{x}$

$$I_{raw}(\mathbf{x}) = \int d\boldsymbol{l} e^{-\imath \mathbf{Q}_h \cdot \boldsymbol{l}} \gamma(\boldsymbol{l}, t) S(\mathbf{x} - \boldsymbol{l}; R), \tag{2.58}$$

where γ is the ocean surface reflectivity, S is the SAR signal spreading function, and R is the slant-range distance of the imaged object. At the ground-range reference point $\mathbf{x}_o$, the ocean surface reflectivity is

$$\gamma(\mathbf{x}_o, t) = \int d\mathbf{x} \delta(\mathbf{x} + \mathbf{k}_h \frac{k_z}{k_h^2} \eta(\mathbf{x}, t) - \mathbf{x}_o) F(\mathbf{x}, t), \tag{2.59}$$

with F being the source function defined as in (2.27). As in the backscatter model described in section 2.3.1, changing the frame of reference using a Lagrangian surface (i.e. $\tilde{\mathbf{x}} = \mathbf{x} + \boldsymbol{\xi}$) , (2.58) becomes

$$I_{raw}(\mathbf{x}) = \int d\mathbf{x} e^{-\imath(\mathbf{Q}_h \cdot (\mathbf{x}+\boldsymbol{\xi}) + Q_z \eta)} F(\mathbf{x}, t) J(\mathbf{x}, t) S(\mathbf{x} - \mathbf{k}_h \frac{k_z}{k_h^2} \eta(\mathbf{x}, t) - \boldsymbol{\xi}; R), \tag{2.60}$$

with J being the Jacobian from (2.34).

Using the principle of stationary phase and an appropriate matched filter, the compressed SAR image corresponding to (2.60) is

$$\hat{I}_c(\mathbf{k}) \approx \int d\mathbf{x} e^{-\imath(\mathbf{Q}_h \cdot (\mathbf{x}+\boldsymbol{\xi}) + Q_z \eta)} F(\mathbf{x}, t_s) J(\mathbf{x}, t_s) U(x_s) V(y_s), \tag{2.61}$$

where U and V are radar parameters related to the signal spreading function S, while x_s, y_s, and t_s correspond to the stationary phase values (more details can be found regarding these quantities in [Pedersen et al., 2004]). Using (2.61), the zeroth and first order moments can be computed with

$$m_0 = \int d\mathbf{k} \langle \hat{I}_c(\mathbf{k}) \hat{I}_c^*(\mathbf{k}) \rangle = \int d\mathbf{x} e^{-\imath \mathbf{Q}_h \cdot \mathbf{x}} \langle e^{\imath(\zeta(\mathbf{0}) - \zeta(\mathbf{x}))} f(\mathbf{x}) f^*(\mathbf{0}) \rangle, \tag{2.62}$$

and

$$m_1 = \int d\mathbf{k} k_y \langle \hat{I}_c(\mathbf{k}) \hat{I}_c^*(\mathbf{k}) \rangle = -\frac{1}{2} \int d\mathbf{x} e^{-\imath \mathbf{Q}_h \cdot \mathbf{x}} \langle e^{\imath(\zeta(\mathbf{0}) - \zeta(\mathbf{x}))} f(\mathbf{x}) f^*(\mathbf{0}) (\dot{\zeta}(\mathbf{x}) + \dot{\zeta}(\mathbf{0})) \rangle. \tag{2.63}$$

In both (2.62) and (2.63), $\zeta = \mathbf{Q}_r \cdot \boldsymbol{\chi}$, f is defined as in (2.36), and k_y is a component of the vector $\mathbf{k}_h$ (i.e. $\mathbf{k}_h = (k_x, k_y)$). The D_c (in unit of Hertz) can now be found

$$D_c = \frac{1}{2\pi} \frac{m_1}{m_0} = \frac{1}{2\pi} \frac{\int d\mathbf{x} e^{-\imath \mathbf{Q}_h \cdot \mathbf{x}} \langle e^{\imath(\zeta(\mathbf{0}) - \zeta(\mathbf{x}))} f(\mathbf{x}) f^*(\mathbf{0}) (\dot{\zeta}(\mathbf{x}) + \dot{\zeta}(\mathbf{0})) \rangle}{\int d\mathbf{x} e^{-\imath \mathbf{Q}_h \cdot \mathbf{x}} \langle e^{\imath(\zeta(\mathbf{0}) - \zeta(\mathbf{x}))} f(\mathbf{x}) f^*(\mathbf{0}) \rangle}. \tag{2.64}$$

Note that the denominator of (2.64) closely resembles (2.33). Just as the computation of (2.33) makes use of transfer functions, the same method is applied to compute the

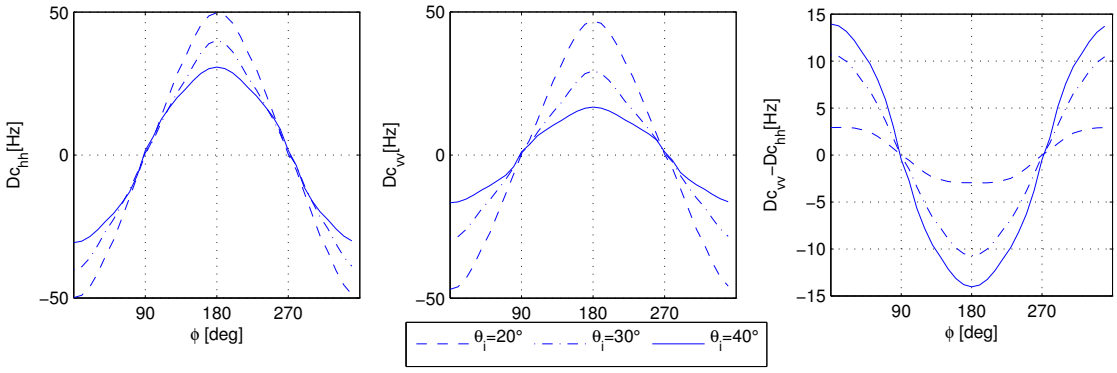

Figure 2.11: Simulated D_{cHH} and D_{cVV} based on the GCM for three incidence angles at C-band (f=5.4 GHz). Selected u_{10} is 12 m/s. The third plot represents the polarization residual Doppler frequency (i.e. $D_{cVV} - D_{cHH}$).

Fourier kernel of the numerator in (2.64) where

$$\begin{aligned}
\langle e^{\imath(\zeta(\mathbf{0})-\zeta(\mathbf{x}))} f(\mathbf{x}) f^*(\mathbf{0})(\dot{\zeta}(\mathbf{x}) + \dot{\zeta}(\mathbf{0}))\rangle = e^{\varphi_{\zeta\zeta}(\mathbf{x})-\varphi_{\zeta\zeta}(\mathbf{0})} \\
[\imath f^{(0)} \varphi_{\dot{\zeta}\zeta}(\mathbf{x})(f^{*(\mathbf{0})} - \imath(\varphi_{\zeta f^{(1)}}(\mathbf{x}) - \varphi_{\zeta f^{(1)}}(\mathbf{0}))) \\
-\imath f^{*(0)} \varphi_{\zeta\dot{\zeta}}(\mathbf{x})(f^{(\mathbf{0})} + \imath(\varphi_{f^{(1)}\zeta}(\mathbf{x}) - \varphi_{f^{(1)}\zeta}(\mathbf{0}))) \\
-f^{(0)} \varphi_{\zeta\dot{\zeta}}(\mathbf{x})(\varphi_{\zeta f^{(1)}}(\mathbf{x}) - \varphi_{\zeta f^{(1)}}(\mathbf{0})) \\
-f^{*(0)} \varphi_{\dot{\zeta}\zeta}(\mathbf{x})(\varphi_{f^{(1)}\zeta}(\mathbf{x}) - \varphi_{f^{(1)}\zeta}(\mathbf{0})) \\
+f^{*(0)}(\varphi_{f^{(1)}\dot{\zeta}}(\mathbf{x}) + \varphi_{f^{(1)}\dot{\zeta}}(\mathbf{0})) \\
+f^{(0)}(\varphi_{\dot{\zeta}f^{(1)}}(\mathbf{x}) + \varphi_{\dot{\zeta}f^{(1)}}(\mathbf{0})) \\
-\imath(\varphi_{f^{(1)}\dot{\zeta}}(\mathbf{x}) + \varphi_{f^{(1)}\dot{\zeta}}(\mathbf{x}))(\varphi_{\zeta f^{(1)}}(\mathbf{x}) - \varphi_{\zeta f^{(1)}}(\mathbf{0})) \\
+\imath(\varphi_{\dot{\zeta}f^{(1)}}(\mathbf{x}) + \varphi_{\dot{\zeta}f^{(1)}}(\mathbf{x}))(\varphi_{f^{(1)}\zeta}(\mathbf{x}) - \varphi_{f^{(1)}\zeta}(\mathbf{0})) \\
+\imath\varphi_{f^{(1)}f^{(1)}}(\mathbf{x})(\varphi_{\dot{\zeta}\zeta}(\mathbf{x}) - \varphi_{\zeta\dot{\zeta}}(\mathbf{x})) \\
+\imath(\varphi_{\dot{\zeta}\zeta}(\mathbf{x}) - \varphi_{\zeta\dot{\zeta}}(\mathbf{x}))(\varphi_{f^{(1)}\zeta}(\mathbf{x}) - \varphi_{f^{(1)}\zeta}(\mathbf{0})) \\
(\varphi_{\zeta f^{(1)}}(\mathbf{x}) - \varphi_{\zeta f^{(1)}}(\mathbf{0}))].
\end{aligned} \tag{2.65}$$

where φ_{ab} are covariances requiring the same transfer functions as for the backscatter model [i.e. (2.56) and (2.57)], as well as

$$T_{\dot{\zeta}}(\mathbf{k}) = -\imath(gk)^{1/2} T_{\zeta}(\mathbf{k}). \tag{2.66}$$

Figure 2.11 shows simulated D_c for both HH and VV polarizations, for three incidence angles, with a 12 m/s u_{10} at C-band (f=5.4 GHz). Note that D_{cHH} is always greater than D_{cVV}. This observation agrees with the result from (2.64), where the D_c is essentially weighted by the NRCS: as shown in Fig. 2.10 and given the selected incidence angles, σ^o_{HH} is always smaller than σ^o_{VV}, which in turn makes D_{cHH} greater than D_{cVV}.

The third plot of Fig. 2.11 represents the difference between D_{cVV} and D_{cHH} which we call the polarization residual Doppler frequency. In the following chapter, this metric is analyzed and used in a wind retrieval scheme. Chapter 5 also provides analysis of the use of an improved Lagrangian implementation which includes the skewness component discussed in chapter 4. It also contains a study on the effect of wave breaking to D_c measurements.